Impact of Ordering on the Reactivity of Mixed Crystals of Topological Insulators with Anion Substitution: Bi_2SeTe_2 and Sb_2SeTe_2

Andrey A. Volykhov[1,2], Alexander S. Frolov[1,3], Vera S. Neudachina[1], Nadezhda V. Vladimirova[1], Eugene Gerber[1], Carolien Callaert[4], Joke Hadermann[4], Nikolay O. Khmelevsky[5], Axel Knop-Gericke[6], Jaime Sánchez-Barriga[7], Lada V. Yashina[1,3*]

1) Department of Chemistry, Lomonosov Moscow State University, Leninskie Gory 1/3, 119991 Moscow, Russia
2) Kurnakov Institute of General and Inorganic Chemistry RAS, Leninsky Avenue 31, 119991 Moscow, Russia
3) N.N. Semenov Federal Research Center for Chemical Physics, Kosygina Street 4, 119991 Moscow, Russia
4) EMAT, Department of Physics, University of Antwerp, Groenenborgerlaan 171, 2020 Antwerp, Belgium
5) Moscow State University of Technology ''STANKIN'', Vadkovsky side-street 1, 127994 Moscow, Russia
6) Fritz-Haber-Institut der Max-Planck-Gesellschaft, Faradayweg 4-6, 14195, Berlin, Germany
7) Helmholtz-Zentrum Berlin, Albert-Einstein-Str. 15, D-12489 Berlin, Germany
*Corresponding author. E-mail: yashina@inorg.chem.msu.ru

Abstract

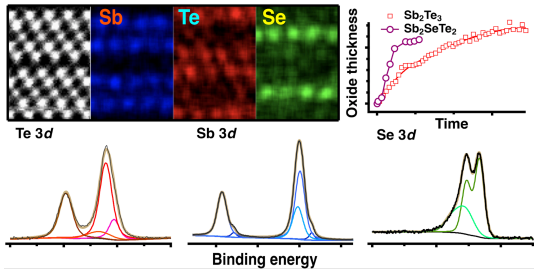

Topological insulators (TIs) are among the most intriguing materials of the 21st century. Tetradymite type binary chalcogenides of bismuth and antimony, as well as their mixed crystals, belong to prototypical TIs. Potential device applications of these materials require in-depth knowledge of their stability in the ambient atmosphere and other media maintained during their processing. Here we investigated the reactivity of mixed crystals with anion substitution, $Bi_2(Se_{1-x}Te_x)_3$ and $Sb_2(Se_{1-x}Te_x)_3$, towards molecular oxygen using both *in situ* and *ex situ* X-ray photoelectron spectroscopy. The results indicate that, in contrast to cation substitution, partial substitution of tellurium by selenium atoms leads to anomalously high surface reactivity, which even exceeds that of the most reactive binary constituent. We attribute this effect to anion ordering that essentially modifies the bond geometry, especially the respective bond angles as modeled by DFT.

Introduction

The discovery of topological insulators (TIs) is one of the most prominent events in 21st century physics [1,2]. Novel physical phenomena observed for TIs construct a platform for creating entirely new electronic devices [3-6]. In contrast to trivial insulators, the appearance of spin-polarized electronic states inside the bulk band gap at the surface or interface with a trivial insulator is caused by band inversion due to strong spin-orbit coupling. The surface of such materials is highly conductive, and the surface electrons that move in the opposite directions also have opposite spins, which allows managing electronic and spin transport. The surface states are protected by the time-reversal symmetry; they are not influenced by any perturbations such as surface defects or non-magnetic impurities.

One of the most studied classes of TIs is tetradymite type compounds with a single Dirac cone located at the Γ point of the surface Brillouin zone, such as Bi_2Te_3, Bi_2Se_3, Sb_2Te_3, as well as various ternary compounds and solid solutions with a similar structure [7]. Solid solutions are of special interest because all relevant parameters such as the Dirac point position, Fermi level energy, and bandgap can be tuned precisely by varying their composition [8-11]. This approach has been successfully applied to produce materials with low bulk conductivity: Bi_2SeTe_2, Sb_2SeTe_2, Bi_2Te_2S, $Bi_{1.5}Sb_{0.5}Te_{1.7}Se_{1.3}$, $Bi_2Te_{1.6}S_{1.4}$ [9,11-21], which is a prerequisite to implement the topological properties in electron transport phenomena. Anion substitution from a certain perspective appears to be more promising than the cation one since it grants a better possibility to increase the band gap [9,11].

In addition to the low bulk conductivity required for TI applications, the Bi_2SeTe_2 phase is of interest for detailed investigation due to a number of unique properties; for instance, a monolayer of Bi_2SeTe_2 has the smallest thermal conductivity among 2D materials [22]. For a similar antimony compound, Sb_2SeTe_2, large linear magnetoresistance with extremely low mobility was measured [17, 23-24]. Based on Sb_2SeTe_2 nanoflakes, a high-performance visible light photodetector was designed [19].

Upon mixing, the atomic positions can either be statistically filled or ordered in a certain way. For a layered structure in an extreme case of specific stoichiometry and 100 % occupation of positions within the individual layers, ternary compounds can be formed; for example, the tetradymite phase of Bi_2STe_2. Generally, for any ternary mixed crystals, either with cation or anion substitution, the situation may vary from pure statistical occupation to a complete ordering depending on the composition and a thermodynamically predetermined ordering tendency. The absence of any cation ordering has been demonstrated earlier, for instance, for the Bi_2Te_3-Sb_2Te_3 solid solutions [25]. It is not surprising since all cation positions are equivalent, and from the thermodynamics viewpoint, mixed crystals belong to the ideal solid solution. In contrast to this, anion ordering is typically observed for solid solutions with the tetradymite structure [7, 16]. In the structure, there are two different anion positions (1/3 of inner positions inside of the quintuple layer (QL) and 2/3 of outer positions); the intralayer position is more energetically favorable for smaller anions [7, 26] as schematically presented in Fig. 1a. Despite an ideal and complete mixing in the Bi_2Se_3-Bi_2Te_3 system (see Fig.1b) and linear concentration dependence of the lattice parameter *a* (Fig. 1c), the Bi_2SeTe_2 phase is formed where almost all intralayer anion positions are occupied by Se atoms, while the positions at the surface of the QLs are occupied by Te (there is some disordering between the positions though it does not exceed 10% [13]). In another system with anion substitution, Sb_2Se_3-Sb_2Te_3, the solubility is limited; mixed crystals exist in the range of 40-100 mol.% Sb_2Te_3, as it is shown in Fig.2a. Such solid solutions show ideal behavior as it follows from the fact that lattice constant variation in Fig. 2b obeys Vegard's rule. Similar to the Bi-based system, it is reasonable to assume that a Sb_2SeTe_2 compound forms with Se occupying the intralayer position, although there have been no experimental confirmations so far [7].

Device applications of these materials require deep knowledge of their stability towards the ambient atmosphere and other media used in material processing. It has already been well established that the reactivity of Bi_2Se_3 to oxygen is very low so that a freshly cleaved surface would show bright RHEED and ARPES patterns [27-29]. Bi_2Te_3 and especially Sb_2Te_3 are much more reactive [29-31]. Therefore, their preparation and processing conditions should be carefully controlled. For mixed crystals with cation substitution, the reactivity can be predicted, as we showed in Ref. [25]; it is an intermediate between the counterparts. In particular, it is determined by the number of anion atoms in the very surface layer bonded to at least one more reactive cation (Sb) atom.

Although certain fragmentary reports on the surface oxidation of the mixed crystals with anion substitution are available [32,33], their reactivity has not yet been evaluated comprehensively. One can expect sophisticated behavior taking into account the ordering, which leads to the prevalence of the more reactive (Te) anion in the very surface layer. Here we focus on the correlation between the reactivity of the mixed crystals and that of their binary constituents, as well as on the anion ordering effect if any. For this reason, the compositions corresponding to the maximum ordering, Bi_2SeTe_2 and Sb_2SeTe_2, were under our particular interest.

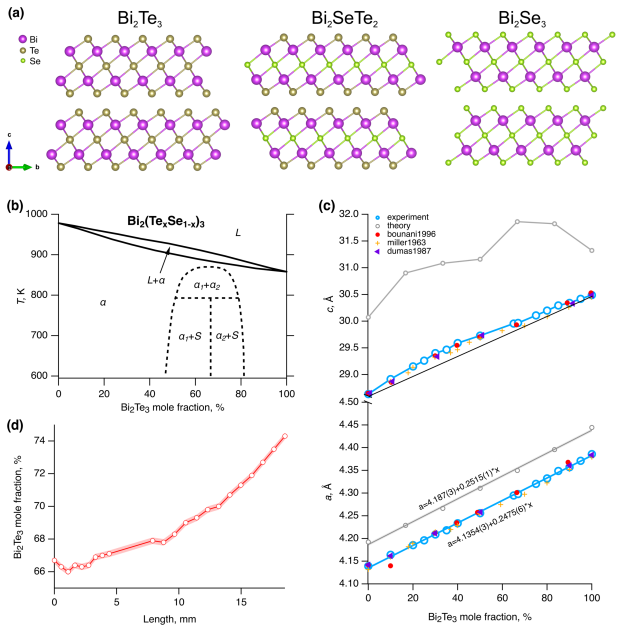

Fig. 1. (a) Crystal structure, (b) Phase diagram of the Bi_2Se_3-Bi_2Te_3 system [35-38]; (c) Dependence of the *a* and *c* unit cell parameters on the composition of the Bi_2Se_3-Bi_2Te_3 solid solutions (our experimental and literature data [36-38]); (d) Bi_2Te_3 fraction distribution along the Bi_2SeTe_2 crystal length according to the XRF data.

Methods

≈10 g Bi_2SeTe_2 and Sb_2SeTe_2 crystals were grown from the melt by the Bridgman method using a procedure similar to that described in Ref. [34]. The melt composition was adjusted to $Bi_{2.1}(Te_{0.75}Se_{0.25})_3$ based on the liquidus and solidus lines in the equilibrium phase diagrams (Figs. 1b and 2a). In the case of Sb_2SeTe_2 we used a $Sb_2(Te_{0.7}Se_{0.3})_3$ melt taking into account the fact that for this solid solution, the crystal composition is always close to the melt composition due to the tendency to melt overcooling by analogy with $(Bi,Sb)_2Te_3$ [42]. The crystal growth took up to 7-9 days and was performed at a pulling rate of 0.75 cm/day. The temperature gradient during growth was set to be 10 K/cm. In addition, a single crystal of $Bi_2(Se_{1-x}Te_x)_3$ (x=0.33) (a solid solution, not a compound) was grown under conditions similar to the above-described ones as a comparison sample for the surface reactivity studies; the corresponding $Sb_2(Se_{1-x}Te_x)_3$ is two-phase according to the phase diagram in Fig. 2a and, therefore, was not investigated. Furthermore, reference crystals of binary compound Bi_2Te_3, Bi_2Se_3, Sb_2Te_3, and Sb_2Se_3 were also grown using a similar procedure from melts containing 60.6 at.%Te, 60 at.%Se, 56 at.%Se, 60 at.%Se, correspondingly.

The crystals obtained were characterized by XRF and additionally by XRD. The XRF measurements were performed using a Bruker Mistral-M1 microfocused system equipped with an XFlash 30mm^2 detector; the concentrations were determined using XSpect software by determining the area of individual peaks using the external standard model. 4-7 measurements were taken for each crystal. The average composition distribution along the crystal length for Bi_2SeTe_2 and Sb_2SeTe_2 determined by XRF is illustrated in Figs. 1d and 2c; it appears to vary gradually for Bi_2SeTe_2. Therefore, an excess of Bi does not provide a uniform distribution of crystal composition as we expected by analogy with Ref. [34]. For further oxidation experiments, we used the initial part of the ingot, where the composition corresponds to the compound stoichiometry. In contrast to this, Sb_2SeTe_2 is uniform in composition due to kinetic reasons. The Sb_2Te_3 content in the grown crystal is somewhat higher (around 71%) than that of Sb_2SeTe_2 (67%); however, there are no indications of any second phase in either XRD or TEM data (see below for more detail). Therefore, excessive Te is probably present in small quantities within the inner layer. Both crystals possess a high carrier concentration of ~10^{18} cm^{-3}, with Bi_2SeTe_2 being *n*-type and Sb_2SeTe_2 being *p*-type.

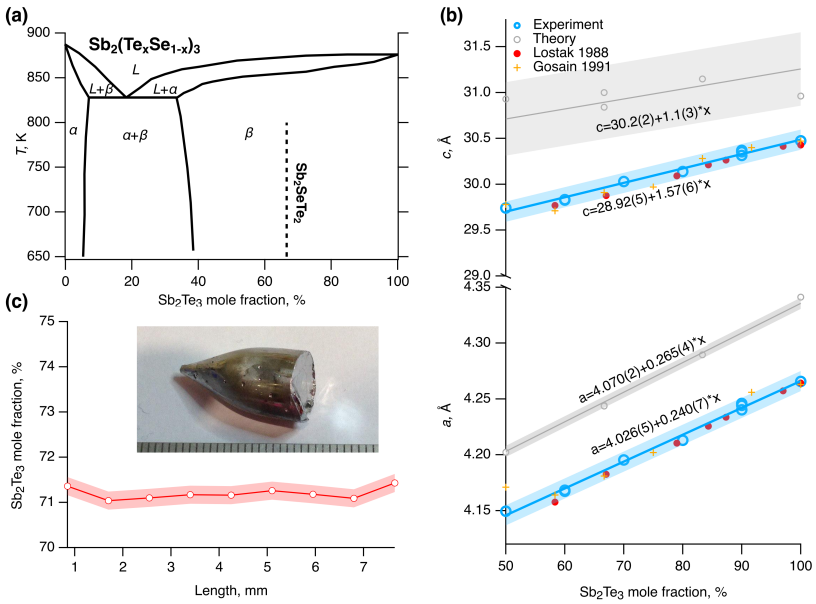

Fig. 2. (a) Phase diagram of the Sb_2Se_3-Sb_2Te_3 system [39-41]; (b) Dependence of the a and c cell parameters on the composition of the Sb_2Se_3-Sb_2Te_3 solid solutions (our experimental and literature data [40-41]); (c) Sb_2Te_3 fraction distribution along the Sb_2SeTe_2 crystal length according to the XRF data;

For the high-angle annular dark-field scanning transmission electron microscopy (HAADF–STEM) imaging and energy- dispersive X-ray (EDX) mapping, cross-sectional samples were prepared on a Cu support by focused ion beam (FIB) milling. The HAADF–STEM and EDX data were acquired on an aberration-corrected Thermo Fischer Scientific Titan transmission electron microscope operating at 200 kV and equipped with a Super-X four EDX detector. We performed a detailed EDX investigation to obtain a rough estimate of the layer occupation in Te/Se layers. We followed a similar procedure described by Lu *et al.* [43,44], using the Sb-L (6.603 keV), Te-L (3.767 keV), and Se-K (11.210 keV) lines. First, we average the atomic resolution map to increase the signal to noise ratio. Next, we fit the line profile of the elemental maps of the mixed positions with a combination of Gaussian functions using the program Fityk [45] The FWHM of the Gaussian peaks for each element was constrained to have the same value for the different layers. Small differences can occur because the FWHM depends on the beam spreading and channeling, which on its own depends on the chemical distribution of the column [44]. However, thin film conditions weaken the dependence. The fitted FWHM of Te-L is 0.27 nm and of Se-K is 0.25 nm. Then, we determine our own k factors of the Cliff-Lorimer method [46] –assuming thin film conditions- which is the scaling factor between the concentration ratio of two elements, C_{Te}/C_{Se} , and their corresponding characteristic X-ray intensity ratio I_{Se}/I_{Te}: $\frac{C_{Te}}{C_{Se}} = k_{Te,Se}\frac{I_{Te}}{I_{Se}}$ .The counts ratio I_{Te}/I_{Se} is determined by taking the ratio of the sum of the areas under the Gaussian peaks of Te and Se. The concentration ratio in atomic percent, C_{Te}/C_{Se}, was obtained from the STEM-EDX data. Knowing the k factors we can use the formulae $\frac{C_{Te}}{C_{Se}} = k_{Te,Se}\frac{I_{Te}}{I_{Se}}$, combined with '$C_{Te}+C_{Se}$ =1' to determine the layer composition of the chemically different Te/Se layers. The error is calculated through error propagation with the k factor variation Δk/k ~0.1 and assuming that the error on the counts is equal to $\sqrt{I}$. The count variation (ΔI/I) is thus negligible compared to the k factor variation when using a reasonable amount of counts per element.

Polycrystalline homogeneous alloys (2g samples) of $Bi_2(Se_{1-x}Te_x)_3$ and $Sb_2(Se_{1-x}Te_x)_3$ were prepared in the whole range of compositions by direct melting of grounded elemental substances (5-6N purity) in evacuated sealed ampoules with subsequent quenching and annealing at $T=T_m$-50K during a week for homogenization. For XRD, the powdered samples were additionally annealed in evacuated sealed ampoules at 300^0C to eliminate mechanical stress. They were investigated by XRD using a PANalytical Empyrean diffractometer equipped with a PSD Pixel3D detector in the 2θ range of 9-100^0 with a step of

0.013^0. The obtained data were treated within the WinXPow software package using the ICDD PDF-2 database.

The core-level photoemission studies were carried out using several facilities of Helmholtz−Zentrum Berlin (HZB), Germany. The NAP XPS *in situ* data were obtained at the ISISS beamline using a station equipped with a SPECS Phoibos 150 NAP analyzer under the oxygen pressure of 0.5 mbar. The crystals were cleaved in vacuum, and then oxygen was admitted to the system. The Sb 3d, Te 3d, Bi 4f, Se3d, and O 1s spectra were recorded at an electron kinetic energy of 200 eV. We used the same kinetic energy for all elements to quantify composition correctly important and to find a quantitative correlation between the spectral components related to different elements at the same depth. The kinetic energy of 200 eV provides high surface sensitivity. It is crucial that 200 eV corresponds to the minimal energy at which the theoretical cross sections of Yeh and Lindau work [47].

For *ex situ* measurements, where the reaction is considered as "frozen" in UHV, the crystals were cleaved under atmospheric conditions and exposed to air at controlled humidity of 44% at room temperature with the total exposure time varying between 30 min and 2000 h. The Bi 5d, Se3d, Te 4d, and O 1s spectra were recorded with high surface sensitivity at the Russian−German beamline of HZB using photoelectron kinetic energies of 50 and 100 eV. The XPS spectra acquisition was performed using a SPECS Phoibos 150 electron energy analyzer.

Besides, for extensive *ex situ* studies at high exposures, we did not use sequential exposures to air of the single sample, but a separate sample was prepared for each time point to exclude (to average) possible influence of cleavage accuracy and keeping in UHV. The X-ray photoelectron spectra were taken using a Thermo Scientific K-Alpha laboratory XPS system that employs a monochromated Al Kα X-ray source. The spectra of analytical lines (Bi 4f, Se 3d, Te $3d_{5/2}$, Sb 3d, O 1s) were taken at the pass energy of 20 eV.

All photoemission spectra were fitted by Gaussian/Lorentzian convolution functions with simultaneous optimization of the background parameters using Unifit 2014 software. The background was modeled using a combination of Shirley- and Tougaard-like backgrounds.

Theoretical modeling was performed within the DFT approach using the PW-GGA method (VASP code [48−50]). Lattice vectors and positions of all atoms were optimized. The first Brillouin zone integrations were made using the Monkhorst–Pack approximation [51]; a 7x7x7 k-points mesh was used for calculations without a supercell, 3x7x7 – for calculations with a 2x1x1 supercell. Core-level shifts were calculated in the initial-state approximation as a variation of electrostatic potentials at the atomic centers. The plane-wave energy cutoff was chosen as 400 eV. Both cell and ion relaxation were performed until residual forces fell below 10^{-3} eV $Å^{-1}$.

Results and Discussion

The *in situ* results obtained for Bi_2SeTe_2 and Sb_2SeTe_2 at a constant oxygen pressure of 0.5 mbar are shown in Figs 3, 4. The experiments were performed under conditions similar to our earlier *in situ* oxidation study of Bi_2Te_3 and Sb_2Te_3 binary compounds [25, 29]. Typically, the *in situ* oxidation results do not indicate the presence of any induction period, and oxidation proceeds faster compared to the *ex situ* experiments due to additional oxygen activation by photons.

Fig. 3a-c demonstrates examples of typical *in situ* spectra corresponding to certain oxygen exposure times. In detail, the oxidation leads to an appearance of an intense Te II component in the Te 3d spectra with a chemical shift (ChS) of +3.52 eV compared to the unoxidized state Te I; Te II corresponds to the Te^{+4} state. The chemical shifts for all elements are collected in Table 1. Another weak component, Te III with a chemical shift of +1.36 eV, can be deconvoluted, which corresponds to an intermediate (>0) tellurium oxidation state; its fraction does not exceed 10% at any point of time, it appears at the beginning of the

oxidation process and fully disappears after 1h of the experiment. This feature may correspond to the situation when a single oxygen atom is bonded to tellurium [52]. In contrast to Bi_2Te_3 and Sb_2Te_3 [25], no Te^0 (described earlier as having a chemical shift of +0.6 -0.8 eV) is observed during the Bi_2SeTe_2 oxidation. The Bi 4f spectra (Fig. 3b) reveal a single additional component shifted by +0.8-1.1 eV compared to the clean surface feature Bi I; its binding energy is close to Bi_2O_3 fully in line with what we observed earlier for Bi_2Te_3 [29]. The Bi II shift relatively to Bi I initially increases but stabilizes at +1.1 eV after approximately 0.5 h of oxidation. Although this behaviour can be described by the introduction of the additional component, we consider it as the permanent variation of Bi effective charge upon oxidation, which is typical for cations in contrast to anions. It should be noted that the Se 3p line overlaps the Bi 4f spectra, but its intensity is negligible under the given experimental conditions. Some selenium oxidation is observed during the experiment (Fig. 3c), with two new components arising: a weak intermediate Se III (+1.63 eV shift relative to the unoxidized state) and Se II (+4.96 eV). The Se III binding energy corresponds to an intermediate oxidized state (similar to Te III), while Se II corresponds to Se^{+4}. It appears that the oxidation of selenium atoms begins later than that of Bi and Te atoms (see Fig. 2d-f). First, only the Se III component is observed. However, its fraction does not change with time; during further oxidation, only the Se II content rises. The O 1s spectrum (see Fig. S1 in the SI file) includes two intense components related to oxide species (529.9 and 530.8 eV) and a third minor component at about 532 eV observed at the earlier stages of the oxidation and probably associated with some peroxide species. It should be noted that the overall selenium content in the oxidized layer is minimal and does not exceed 1.5% (see Fig. 3g). At the same time, the layer of Bi_2SeTe_2 near the oxide-crystal interface becomes enriched in Se as it follows from composition quantification based on intensities of components Bi I, Se I, Te I (see Fig. S2 in the SI file). Therefore, redistribution of Se and Te takes place between the crystal near the interface and the oxide layer; the latter is enriched in a more reactive component due to the higher benefit of the Te-O bond formation (SeO_2 has a formation enthalpy of -226 kJ/(mole Se) [53] against –(284-289) kJ/(mole Bi) for Bi_2O_3 [53,54] and -321 kJ/(mole Te) for TeO_2 [55]). It should be noted that similar redistribution behavior was observed earlier for the $(Bi_{1-x}Sb_x)_2Te_3$ mixed crystals where the oxide layer is enriched in Sb, while the underlying crystal contains more Bi at the interface than in bulk [25,56].

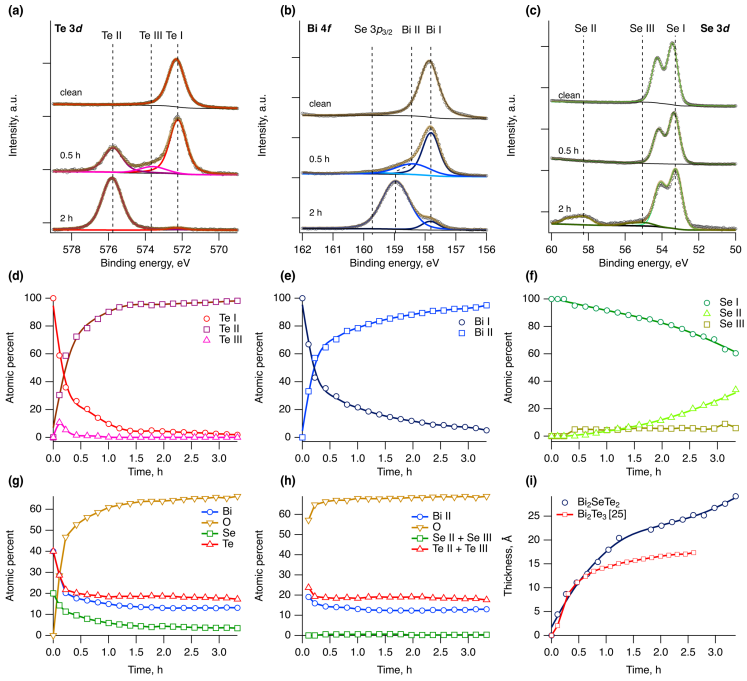

Fig. 3. *In situ* oxidation results for Bi_2SeTe_2 at an oxygen pressure of 0.5 mbar and *T*=298K; kinetic energy is 200 eV: (a)-(c) Te $3d_{5/2}$, Bi $4f_{7/2}$, Se 3d spectra at similar oxygen exposures 0.5 h (top) and 2 h (bottom), respectively; (d)-(f) Variation of the spectral component fraction with time; (g) Time dependence of the surface composition; (h) Time dependence of the oxidized layer composition; (i) Oxide layer thickness vs. oxidation time as compared to similar results obtained for Bi_2Te_3 under same conditions [25].

Table 1. Chemical shifts for spectral features that arise during the oxidation calculated relative to the clean surface (eV)

	Bi I	Bi II	Sb I	Sb II	Te I	Te II	Te III	Te IV	Se I	Se II	Se III	Se IV
Bismuth compounds - *in situ* data												
Bi_2SeTe_2	0	1.1	n/a	n/a	0	3.5	1.4	–	0	5.0	1.6	-
Bi_2Te_3	0	1.4	n/a	n/a	0	3.8	1.3	0.8	n/a	n/a	n/a	n/a
Bismuth compounds - *ex situ* data												
Bi_2SeTe_2	0	1.1	n/a	n/a	0	3.6	–	–	0	5.0	–	-
Bi_2Se_3	0	1.3	n/a	n/a	n/a	n/a	n/a	n/a	0	5.0	1.6	-
Bi_2Te_3	0	1.5	n/a	n/a	0	3.8	-	–	n/a	n/a	n/a	n/a
Antimony compounds - *in situ* data												
Sb_2SeTe_2	n/a	n/a	0	1.4	0	3.8	1.1	0.6	0	-	–	0.85
Sb_2Te_3	n/a	n/a	0	1.6	0	3.8	1.1	0.6	n/a	n/a	n/a	n/a
Antimony compounds - *ex situ* data												
Sb_2SeTe_2	n/a	n/a	0	1.4	0	3.8	–	0.7	0	-	–	0.7
Sb_2Se_3	n/a	n/a	0	1.2	n/a	n/a	n/a	n/a	0	-	1.4	0.6
Sb_2Te_3	n/a	n/a	0	1.6	0	3.8	-	0.7	n/a	n/a	n/a	n/a

Fig. 3g presents the surface composition variation during the oxidation process; a quick oxygen content rise is observed, while tellurium oxidizes slower than bismuth. As a result, the surface is enriched in Te compared to Bi and especially to Se. The oxidized layer composition calculated from all oxidation-related spectral components stabilizes after 0.5-1 h of oxidation and further remains constant; it can be approximately described as $Bi_2Te_3O_{11}$. The oxygen content somewhat exceeds that expected for a mixed Bi_2O_3-TeO_2 oxide. The oxide layer thickness was calculated using the modified Hill equation similar to [25, 29]:

$$d = L_o \ln(\frac{a_s L_s I_o}{a_o L_o I_s} + 1), \qquad (1)$$

where d is the oxidized layer thickness; a_o, a_s is the element (Te) fraction in the oxide and the substrate, respectively; L_o, L_s corresponds to the inelastic mean free path (IMFP) in the oxide and the substrate, respectively; I_o, I_s are photoemission line intensities for the oxide (Te II, Te III) and the substrate (Te I).

The obtained oxide layer thickness variations illustrated in Fig. 2i evidence that Bi_2SeTe_2 is more reactive towards oxygen than Bi_2Te_3, which is surprising and appears to be anomalous as the surface reactivity increases when a much less reactive component, Bi_2Se_3, is added. The bismuth selenide surface is known to be oxidation resistant at room temperature during *ex situ* studies, in dry air it does not oxidize even after 1 year of exposure [27, 29] (see Supporting Information file). In contrast to this, for cation substitution, e.g., for the $(Bi_{1-x}Sb_x)_2Te_3$ solid solutions [25], as mentioned above, there is no such effect, and the solid solutions have intermediate reactivity compared to the respective binary compounds.

In the case of Sb_2SeTe_2, the typical spectra are illustrated in Fig. 4a-c. Upon oxidation, three additional spectral features, Te II-IV, appear with chemical shifts of +0.6 (Te IV), +1.1 (Te III), and +3.8 eV (Te II). Te III and Te IV are related to intermediates, as discussed above for Bi_2SeTe_2. Remarkably, Te II corresponding to the +4 state arises with some delay; this behavior is similar to Sb_2Te_3. In the Sb 3d spectra, the Sb II component has binding energy close to that in Sb_2O_3. In the Se 3d spectra, the intermediate Se IV component is intense, whereas Se III and Se II are absent, which is quite different from the Bi_2SeTe_2 oxidation products. The O 1s peak positioned at 530.3 eV is observed, which corresponds to oxide species. Like for Bi_2Te_3, the oxide layer is enriched in Sb compared to the pure surface, and its composition is approximately described by the $Sb_3Te_2O_{12}$ stoichiometry. Based on the obtained results, it appears that the oxidation products for Bi_2SeTe_2 are close to those of Bi_2Te_3, while for Sb_2SeTe_2 they somewhat resemble those of Sb_2Te_3.

One should stress that the Sb_2SeTe_2 oxidation proceeds remarkably faster than that of Sb_2Te_3, similar to the anomalous effect observed for Bi_2SeTe_2 against Bi_2Te_3. At the same time, Sb_2Te_3 is much more reactive than Sb_2Se_3, as it follows from the *ex situ* data presented in Fig.5a, where all binary compounds are compared in their reactivity.

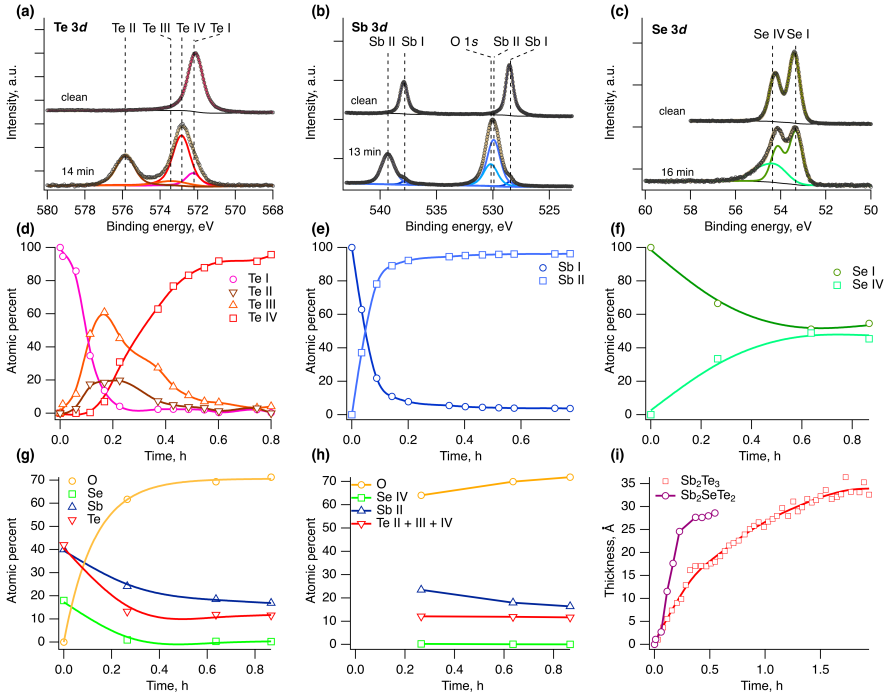

Fig. 4. *In situ* oxidation results for the Sb_2SeTe_2 crystal surface at an oxygen pressure of 0.5 mbar and kinetic energy of 200 eV: (a)-(c) Te $3d_{5/2}$, Bi $4f_{7/2}$, Se 3d spectra at similar oxygen exposures; (d)-(f) Variation of the spectral component fraction with time; (g) Time dependence of the surface composition; (h) Time dependence of the oxidized layer composition; (i) Oxide layer thickness vs. oxidation time as compared to similar results obtained for binary and other ternary compounds measured under similar conditions [25].

It should be noted that, of course, NAP XPS grants the best possibility to study the reaction mechanisms and evaluate the reactivity of any solid materials towards gases. However, it has certain restrictions mostly related to beam activation of the gas molecules (see ESI, Fig. S3). To verify our main finding of *in situ* experiments described above concerning enhanced reactivity of mixed crystals with anion substitution, we performed long-term *ex situ* measurements. For comparison purposes, Bi_2Te_3 surface oxidation was also investigated under the same conditions. The typical spectra and their description are provided in the ESI file, Figs. S4-S6.

Generally, although the oxidation rate is much slower, the spectral features for the spectra obtained *ex situ* are similar to those for the *in situ* experiments (see Table 1) with the exception that some intermediate species were not detected, which is natural and has been observed earlier for binary systems. This correspondence is very important to confirm that the reaction mechanism does not change due to the beam effect.

Our *ex situ* data presented in Fig. 5b (in logarithmic time scale due to significant exposure time range) confirm that the reactivity of Bi_2SeTe_2 (i.e., the exposure at which the oxidation starts) is higher than for both binary constituents, Bi_2Te_3 and Bi_2Se_3, since the oxidation starts earlier and proceeds faster up to the oxide thickness of 1 nm in this case. Furthermore, the oxidation rate is similar to or just slightly lower than that of Bi_2Te_3. For higher Se concentration (see the $Bi_2(Se_{0.67}Te_{0.33})_3$ data provided for comparison in Fig. 5b), the reactivity is remarkably lower, as Se atoms start to fill in the positions in the outer layers of the QL.

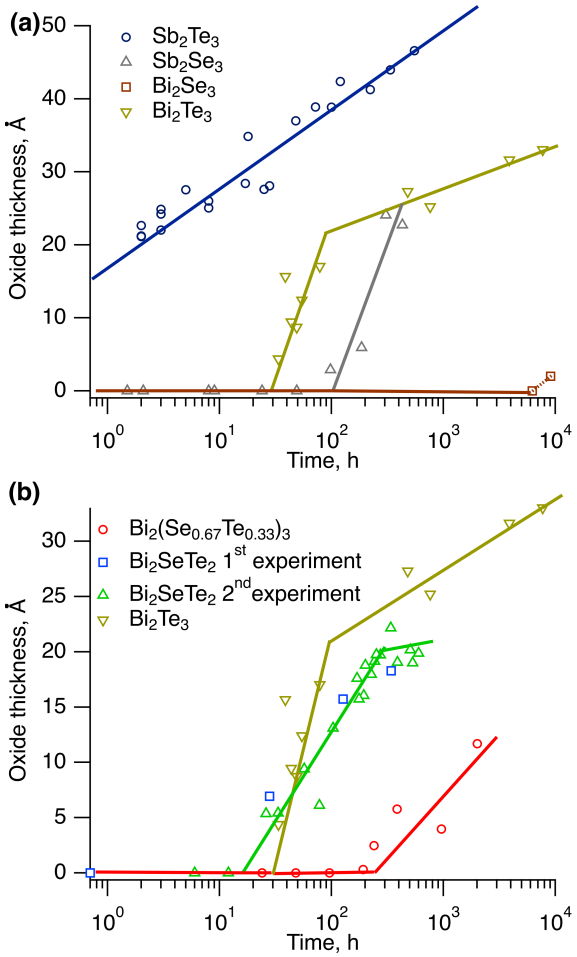

Fig. 5. Oxidation kinetics for the binary compounds (a) and $Bi_2(Se_{1-x}Te)_x$ as compared with Bi_2Te_3 (b)

The upper layer of Bi_2SeTe_2, as mentioned earlier, includes Te atoms with a minor amount (up 10%) of Se atoms [13]; therefore, its reactivity is expected to be similar to that of Bi_2Te_3 or slightly lower. The central layer of each quintuple layer consists of less reactive Se mostly, which, however, does not decrease the reaction rate. For higher Se concentration, the Se atoms also occupy outer positions, and the reactivity decreases as it demonstrated with $Bi_2(Se_{0.67}Te_{0.33})_3$ crystal (see Fig. 5b). We find it intriguingly interesting that the reactivity of both Bi_2SeTe_2 and Sb_2SeTe_2 even slightly enhances that of the most reactive counterpart. The possible reason for such unexpected behavior of Bi_2SeTe_2 and Sb_2SeTe_2 may be lattice distortion caused by the fact that Se and Te occupy individual layers whereas the lattice constants have intermediate values, which reflect both Te layer contraction and Se layer expansion. One should note that covalent bonds are between these layers, and bond lengths may preserve under the contraction/expansion.

To analyze the distortion of the bond geometry cases by ordering for the Bi_2SeTe_2 and Sb_2SeTe_2 phases, we simulated them as well as $Bi_2(Te_xSe_{1-x})_3$ and $Sb_2(Te_xSe_{1-x})_3$ solid solutions of various compositions by DFT with full structural optimization including the lattice constants(see Figs 1b,2b); the obtained results were compared to the literature data for the respective binary compounds (Bi_2Te_3, Bi_2Se_3, Sb_2Te_3; Sb_2Se_3 was not considered as it belongs to a different crystal system). We have considered Bi_2SeTe_2 and Sb_2SeTe_2 phases as fully ordered.

As it was mentioned above, atomic mixing in Bi_2SeTe_2 does not exceed 10 % according to data [13]. For Sb_2SeTe_3, this issue was not studied before. We performed a detailed EDX investigation to obtain a rough estimate of the chemical layer composition of the chemically different Te/Se layers. The results are presented in Fig. 6. For the first look, Se atoms occupy solely central positions in the quintuple layer, whereas Te atoms prefer the outer positions. However, the quantitative analysis performed as described

in the experimental section, reveals some disordering for the occupation of anion positions. In detail, the outer layer contains 14±4% Se, whereas the inner layer is composed of 70±3% Se instead of an ideal 100%. Generally, the disorder level is relatively low and difficult to model. Therefore, as a reasonable simplification for our purpose, the disordering in occupation was disregarded.

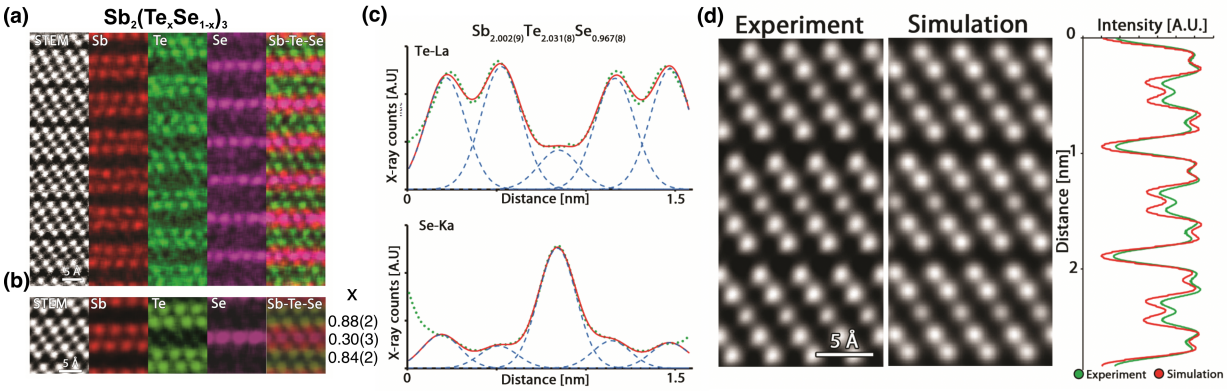

Fig.6. (a) HAADF-STEM cross-sectional image and EDX mapping of the Sb_2SeTe_2 surface, (b) averaged atomic resolution map; (c) Intensity profiles obtained for the averaged map in (b), (d) comparison between the averaged experimental HAADF-STEM image and simulated HAADF-STEM image, simulations are performed with populations given in (b) and using QSTEM [57].

For the compositions of solid solutions other than $(Bi/Sb)_2SeTe_2$, the anion positions in a supercell were populated as follows: Se atoms were substituted in the inner positions first; after the inner positions were fully occupied, substitution in the outer layers started. Since the symmetry of such artificial structure drops, we used mean values of the structural parameters. The lattice constants for the calculated structures are presented in Figs 1c and 2c. Although the absolute values deviate from the experimental ones (since vdW interactions were not included), the computed structures reproduce the linear behavior of lattice constant *a* fully in line with the experimental observations made by us and also indicated in the literature [36-38,40,41]. The *c* parameter demonstrates a deviation from Vegard's law for $Bi_2(Te_xSe_{1-x})_3$. The maximum difference corresponds to the Bi_2Se_2Te composition according to the experimental data in Fig. 1c (presumably due to specific anion ordering in the *c* direction).

The results illustrating the comparison of bond geometry for Bi_2SeTe_2 are presented in Fig. 7 and for Sb_2SeTe_2 in ESI, Fig. S7. In detail, for Bi_2SeTe_2 the Bi-Te bond length is 3.075 Å, which is 0.021 Å (0.7%) shorter than in pure bismuth telluride; the Bi-Se bond length is 3.124 Å, which is 0.018 Å (0.6%) larger than in pure bismuth selenide, respectively. Changes in the bond angle values for the corresponding bonds are much more pronounced: the Te-Bi-Te bond angle changes from 91.74° to 89.87° for the ternary compound, while the Se-Bi-Se angle increases from 84.90° to 88.08°. In the case of Sb_2SeTe_2, the respective bond length changes are even more pronounced: the Sb-Te bond length is 3.009 Å, which is 0.032 Å (1.05%) less than in pure Sb_2Te_3; the Te-Sb-Te angle also decreases from 92.40° to 89.71°. The unit cell parameter *a* for Bi_2SeTe_2, when compared to Bi_2Te_3 and Bi_2Se_3, is 0.4% less than the value calculated according to the Vegard's law, while the *c* parameter is +0.6% as compared to calculated value.

If we compare these results with cation substitution in the $(Bi_{1-x}Sb_x)_2Te_3$ mixed crystals where there is less difference in the *a* cell parameters of the binary constituents (≈3%), and different cations are statistically distributed [25]. For $Bi_2(Te_xSe_{1-x})_3$, the difference in the *a* cell parameters for the binary constituents, namely, Bi_2Te_3 and Bi_2Se_3, amounts to ≈6%, which can cause the above-described calculated bond geometry distortion. The same behavior is observed for Sb_2SeTe_2; the corresponding data are presented in the ESI file.

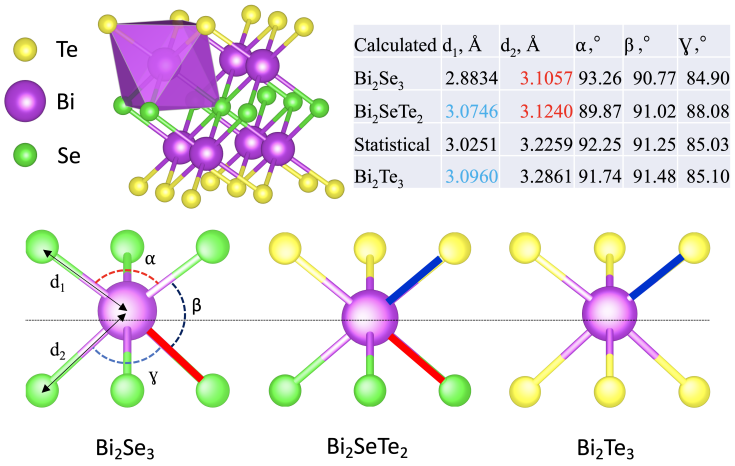

Calculated	d_1, Å	d_2, Å	α,°	β,°	γ,°
Bi_2Se_3	2.8834	3.1057	93.26	90.77	84.90
Bi_2SeTe_2	3.0746	3.1240	89.87	91.02	88.08
Statistical	3.0251	3.2259	92.25	91.25	85.03
Bi_2Te_3	3.0960	3.2861	91.74	91.48	85.10

Fig. 7. Bond geometry in Bi_2SeTe_2 as compared with parent compounds

Conclusions

Anomalously high reactivity in reaction with molecular oxygen was observed for the $Bi_2(Te_xSe_{1-x})_3$ and $Sb_2(Te_xSe_{1-x})_3$ solid solutions based on *in situ* and *ex situ* photoemission experiments: while Bi_2Se_3 is known to be resistant to oxygen at room temperature and Bi_2Te_3 has medium reactivity, Bi_2SeTe_2 surfaces have higher reactivity than that of bismuth telluride. Similar results were obtained for Sb_2SeTe_2. We attribute this effect to cation ordering, which modifies essentially bond geometry, especially bond angles, as modeled by DFT.

Acknowledgments

This work was financially supported by RSF, grant 19-42-06303. A.A.V. acknowledges the individual support grant of the President of the Russian Federation No. MK-899.2018.3 for his theoretical studies. We thank Helmholtz-Zentrum Berlin for granting access to the beamlines RGBL and ISISS. We thank Dr. Anna Makarova and Dr. Juan Velasco-Vélez for their support during measurements. Quantum chemical calculations were performed at "Lomonosov" supercomputer of MSU. J.H. and C.C. acknowledge support from the University of Antwerp through BOF Grant No. 31445.

Author contributions

Lada V. Yashina and Andrey A. Volykhov created general concept and did planning of experiment. Nadezhda V. Vladimirova and Eugene Gerber performed sample preparation and characterization. Andrey A. Volykhov performed DFT calculations and XPS data treatment. Alexander S. Frolov, Vera S. Neudachina, Nikolay O. Khmelevsky, Lada V. Yashina and Jaime Sánchez-Barriga performed photoemission studies. Carolien Callaert, Joke Hadermann did TEM works. Lada V. Yashina, Vera Neudachina, Andrey A. Volykhov, Alexander S. Frolov, Axel Knop-Gericke contributed to the discussion and manuscript writing.

References

[1] M. Z. Hasan and C. L. Kane, Colloquium: Topological insulators, *Rev Mod Phys*, 2010, **82**, 3045–3067.
[2] X.-L. Qi and S.-C. Zhang, Topological insulators and superconductors, *Rev Mod Phys*, 2011, **83**, 1057–1110.
[3] J. E. Moore, The birth of topological insulators, *Nature*, 2010, **464**, 194–198.
[4] B. A. Bernevig, T. L. Hughes and S.-C. Zhang, Quantum Spin Hall Effect and Topological Phase Transition in HgTe Quantum Wells, *Science*, 2006, **314**, 1757–1761.
[5] M. Koenig, S. Wiedmann, C. Bruene, A. Roth, H. Buhmann, L. W. Molenkamp, X.-L. Qi and S.-C. Zhang, Quantum Spin Hall Insulator State in HgTe Quantum Wells, *Science*, 2007, **318**, 766–770.

[6] D.-X. Qu, Y. S. Hor, J. Xiong, R. J. Cava and N. P. Ong, Quantum Oscillations and Hall Anomaly of Surface States in the Topological Insulator Bi2Te3, *Science*, 2010, **329**, 821–824.
[7] J. P. Heremans, R. J. Cava and N. Samarth, Tetradymites as thermoelectrics and topological insulators, *Nat Rev Mater*, 2017, **2**, 17049.
[8] L.-L. Wang and D. D. Johnson, Ternary tetradymite compounds as topological insulators, *Phys Rev B*, 2011, **83**, 241309.
[9] Z. Ren, A. A. Taskin, S. Sasaki, K. Segawa and Y. Ando, Large bulk resistivity and surface quantum oscillations in the topological insulator Bi2Te2Se, *Phys Rev B*, 2010, **82**, 241306.
[10] I. Teramoto and S. Takayanagi, Relations between the electronic properties and the chemical bonding of sbxBi2−xTe3−ySey system, *J Phys Chem Solids*, 1961, **19**, 124–129.
[11] T. Arakane, T. Sato, S. Souma, K. Kosaka, K. Nakayama, M. Komatsu, T. Takahashi, Z. Ren, K. Segawa and Y. Ando, Tunable Dirac cone in the topological insulator Bi2-xSbxTe3-ySey, *Nat Commun*, 2012, **3**, 636.
[12] A. A. Taskin, Z. Ren, S. Sasaki, K. Segawa and Y. Ando, Observation of Dirac Holes and Electrons in a Topological Insulator, *Phys Rev Lett*, 2011, **107**, 016801.
[13] S. Jia, H. Ji, E. Climent-Pascual, M. K. Fuccillo, M. E. Charles, J. Xiong, N. P. Ong and R. J. Cava, Low-carrier-concentration crystals of the topological insulator Bi2Te2Se, *Phys Rev B*, 2011, **84**, 235206.
[14] A. Kadhim, A. Hmood and H. A. Hassan, Thermoelectric generation device based on p-type Bi0.4Sb1.6Te3 and n-type Bi2Se0.6Te2.4 bulk materials prepared by solid state microwave synthesis, *Solid State Commun*, 2013, **166**, 44–49.
[15] H. Ji, J. M. Allred, M. K. Fuccillo, M. E. Charles, M. Neupane, L. A. Wray, M. Z. Hasan and R. J. Cava, Bi2Te1.6S1.4: A topological insulator in the tetradymite family, *Phys Rev B*, 2012, **85**, 201103.
[16] Z. Ren, A. A. Taskin, S. Sasaki, K. Segawa and Y. Ando, Large bulk resistivity and surface quantum oscillations in the topological insulator Bi2Te2Se, *Phys Rev B*, 2010, **82**, 241306.
[17] S.-M. Huang, S.-H. Yu and M. Chou, The linear magnetoresistance from surface state of the Sb2SeTe2 topological insulator, *J Appl Phys*, 2016, **119**, 245110.
[18] S.-M. Huang, S.-J. Huang, Y.-J. Yan, S.-H. Yu, M. Chou, H.-W. Yang, Y.-S. Chang and R.-S. Chen, Highly responsive photoconductance in a Sb 2 SeTe 2 topological insulator nanosheet at room temperature, *Rsc Adv*, 2017, **7**, 39057–39062.
[19] S.-M. Huang, S.-J. Huang, Y.-J. Yan, S.-H. Yu, M. Chou, H.-W. Yang, Y.-S. Chang and R.-S. Chen, Extremely high-performance visible light photodetector in the Sb2SeTe2 nanoflake, *Sci Rep-uk*, 2017, **7**, 45413.
[20] S.-M. Huang, Y.-J. Yan, S.-H. Yu and M. Chou, Thickness-dependent conductance in Sb2SeTe2 topological insulator nanosheets, *Sci Rep-uk*, 2017, **7**, 1896.
[21] E. Papalazarou, L. Khalil, M. Caputo, L. Perfetti, N. Nilforoushan, H. Deng, Z. Chen, S. Zhao, A. Taleb-Ibrahimi, M. Konczykowski, A. Hruban, A. Wołoś, A. Materna, L. Krusin-Elbaum and M. Marsi, Unraveling the Dirac fermion dynamics of the bulk-insulating topological system Bi2Te2Se, *Phys Rev Mater*, 2018, **2**, 104202
[22] B. Xu, L. Song, G. Peng, J. Zhang, S. Ma, Y. Wang and Y. Wang, Thermoelectric performance of monolayer Bi2Te2Se of ultra low lattice thermal conductivity, *Phys Lett A*, 2019, **383**, 125864.
[23] S.-M. Huang, S.-H. Yu and M. Chou, The large linear magnetoresistance in Sb2Se2Te single crystal with extremely low mobility, *Mater Res Express*, 2016, **3**, 126101.
[24] K. Shrestha, V. Marinova, D. Graf, B. Lorenz and C. W. Chu, Large magnetoresistance and Fermi surface study of Sb 2 Se 2 Te single crystal, *J Appl Phys*, 2017, **122**, 125901.
[25] A. A. Volykhov, J. Sánchez-Barriga, M. Batuk, C. Callaert, J. Hadermann, A. P. Sirotina, V. S. Neudachina, A. I. Belova, N. V. Vladimirova, M. E. Tamm, N. O. Khmelevsky, C. Escudero, V. Pérez-Dieste, A. Knop-Gericke and L. V. Yashina, Can surface reactivity of mixed crystals be predicted from their counterparts? A case study of (Bi 1−x Sb x) 2 Te 3 topological insulators, *J Mater Chem C*, 2018, **6**, 8941–8949.
[26] D. West, Y. Y. Sun, H. Wang, J. Bang and S. B. Zhang, Native defects in second-generation topological insulators: Effect of spin-orbit interaction on Bi2Se3, *Phys Rev B*, 2012, **86**, 121201.
[27] V. V. Atuchin, V. A. Golyashov, K. A. Kokh, I. V. Korolkov, A. S. Kozhukhov, V. N. Kruchinin, S. V. Makarenko, L. D. Pokrovsky, I. P. Prosvirin, K. N. Romanyuk and O. E. Tereshchenko, Formation of Inert Bi 2 Se 3 (0001) Cleaved Surface, *Cryst Growth Des*, 2011, **11**, 5507–5514.
[28] H. M. Benia, C. Lin, K. Kern and C. R. Ast, Reactive Chemical Doping of the Bi2Se3 Topological Insulator, *Phys Rev Lett*, 2011, **107**, 177602.

[29] L. V. Yashina, J. Sánchez-Barriga, M. R. Scholz, A. A. Volykhov, A. P. Sirotina, V. Neudachina S., M. E. Tamm, A. Varykhalov, D. Marchenko, G. Springholz, G. Bauer, A. Knop-Gericke and O. Rader, Negligible Surface Reactivity of Topological Insulators Bi 2 Se 3 and Bi 2 Te 3 towards Oxygen and Water, *Acs Nano*, 2013, **7**, 5181–5191.
[30] V. V. Atuchin, V. A. Golyashov, K. A. Kokh, I. V. Korolkov, A. S. Kozhukhov, V. N. Kruchinin, I. D. Loshkarev, L. D. Pokrovsky, I. P. Prosvirin, K. N. Romanyuk and O. E. Tereshchenko, Crystal growth of Bi2Te3 and noble cleaved (0001) surface properties, *J Solid State Chem*, 2016, **236**, 203–208.
[31] A. A. Volykhov, J. Sánchez-Barriga, A. P. Sirotina, V. S. Neudachina, A. S. Frolov, E. A. Gerber, E. Y. Kataev, B. Senkovsky, N. O. Khmelevsky, A. Y. Aksenenko, N. V. Korobova, A. Knop-Gericke, O. Rader and L. V. Yashina, Rapid Surface Oxidation of Sb 2 Te 3 as Indication for a Universal Trend in the Chemical Reactivity of Tetradymite Topological Insulators, *Chem Mater*, 2016, **28**, 8916–8923.
[32] C. R. Thomas, G. Sahasrabudhe, S. K. Kushwaha, J. Xiong, R. J. Cava and J. Schwartz, Topological surface states of Bi 2 Te 2 Se are robust against surface chemical modification: Topological surface states of Bi 2 Te 2 Se are robust against surface chemical modification, *Phys Status Solidi Rrl - Rapid Res Lett*, 2014, **8**, 997–1002.
[33] C. R. Thomas, M. K. Vallon, M. G. Frith, H. Sezen, S. K. Kushwaha, R. J. Cava, J. Schwartz and S. L. Bernasek, Surface Oxidation of Bi2(Te,Se)3 Topological Insulators Depends on Cleavage Accuracy, *Chem Mater*, 2016, **28**, 35–39.
[34] V. I. Shtanov and L. V. Yashina, On the Bridgman growth of lead–tin selenide crystals with uniform tin distribution, *J Cryst Growth*, 2009, **311**, 3257–3264.
[35] S.N. Chizhevskaya, L.Ye. Shelimova, V.I. Kosyakov and V.A. Shestakov, Critical evaluation and optimization of data on the Bi-Te-Se phase diagram and crystal structure of Bi_2Te_4-Bi_2Se_3 alloys *Neorganicheskie Materialy (in Russian)*, 1997, **33**, 903-911.
[36] H. G. Bouanani, D. Eddike, B. Liautard and G. Brun, Solid state demixing in Bi2Se3-Bi2Te3 and Bi2Se3-In2Se3 phase diagrams, *Mater Res Bull*, 1996, **31**, 177–187.
[37] G. R. Miller, C.-Y. Li and C. W. Spencer, Properties of Bi_2Te_3 -Bi_2Se_3 Alloys. *J. Appl. Phys.*, 1963, **34**, 1398.
[38] J. F. Dumas, G. Brun, B. Liautard, J. C. Tedenac and M. Maurin, New contribution in the study of the Bi_2Te_3-Bi_2Se_3 system. *Thermochim. Acta*, 1987, **122**, 135-141.
[39] V. I. Ivliyeva and N. Kh. Abrikosov, Phase equilibrium in systems formed by antimony chalcogenides. *Doklady AN SSSR (in Russian)*, 1964, **159**, 1326–1329.
[40] P. Lošťák, R. Novotný, L. Beneš and S. Civiš, Preparation and some physical properties of Sb2Te3−xSex single crystals, *J Cryst Growth*, 1989, **94**, 656–662.
[41] D. P. Gosain, T. Shimizu, M. Ohmura, M. Suzuki, T. Bando and S. Okano, Some properties of Sb2Te3−xSex for nonvolatile memory based on phase transition, *J Mater Sci*, 1991, **26**, 3271–3274..
[42] N. Kh. Abrikosov, V. F. Bankina, L. A. Kolomoets and N. V. Dzhaliashvili, Deviation of the solid solution from the stoichiometric cross-section Bi_2Te_3-Sb_2Te_3 in the $Bi_{0.5}Sb_{1.5}Te_3$ composition region. *Izv. Akad. Nauk SSSR, Neorg. Mater.*, 1977, **13**, 827-829.
[43] P. Lu, L. Zhou, M. J. Kramer and D. J. Smith, Atomic-scale Chemical Imaging and Quantification of Metallic Alloy Structures by Energy-Dispersive X-ray Spectroscopy, *Sci Rep-uk*, 2014, **4**, 3945.
[44]P. Lu, J. Xiong, M. V. Benthem and Q. Jia, Atomic-scale chemical quantification of oxide interfaces using energy-dispersive X-ray spectroscopy, *Appl Phys Lett*, 2013, **102**, 173111.
[45] M. Wojdyr, Fityk : a general-purpose peak fitting program, *J Appl Crystallogr*, 2010, **43**, 1126–1128.
[46] D. B. Williams and C. B. Carter, Transmission Electron Microscopy, A Textbook for Materials Science, , DOI:10.1007/978-0-387-76501-3.
[47] J. J. Yeh and I. Lindau, Atomic subshell photoionization cross sections and asymmetry parameters: $1 \leqslant Z \leqslant 103$, *Atom Data Nucl Data*, 1985, **32**, 1–155.
[48] G. Kresse and J. Hafner, Ab initio molecular dynamics for liquid metals, *Phys Rev B*, 1993, **47**, 558–561.
[49] G. Kresse and J. Hafner, Ab initio molecular dynamics for open-shell transition metals, *Phys Rev B*, 1993, **48**, 13115–13118.
[50] G. Kresse and J. Hafner, Ab initio molecular-dynamics simulation of the liquid-metal–amorphous-semiconductor transition in germanium, *Phys Rev B*, 1994, **49**, 14251–14269.

[51] H. J. Monkhorst and J. D. Pack, Special points for Brillouin-zone integrations, *Phys Rev B*, 1976, **13**, 5188–5192.
[52] L. V. Yashina, T. S. Zyubina, R. Püttner, A. S. Zyubin, V. I. Shtanov and E. V. Tikhonov, A Combined Photoelectron Spectroscopy and ab Initio Study of the Adsorbate System O 2 /PbTe(001) and the Oxide Layer Growth Kinetics, *J Phys Chem C*, 2008, **112**, 19995–20006.
[53] Database ‘‘Thermodynamic constants of substances’’, http://www.chem.msu.su/cgi-bin/tkv.pl
[54] M. Aspiala, D. Sukhomlinov and P. Taskinen, Standard thermodynamic properties of Bi2O3 by a solid-oxide electrolyte EMF technique, *J Chem Thermodyn*, 2014, **75**, 8–12.
[55] E. H. P. Cordfunke, W. Ouweltjes and G. Prins, Standard enthalpies of formation of tellurium compounds I. Tellurium dioxide, *J Chem Thermodyn*, 1987, **19**, 369–375.
[56] A. P. Sirotina, C. Callaert, A. A. Volykhov, A. S. Frolov, J. Sánchez-Barriga, A. Knop-Gericke, J. Hadermann and L. V. Yashina, Mechanistic Studies of Gas Reactions with Multicomponent Solids: What Can We Learn By Combining NAP XPS and Atomic Resolution STEM/EDX?, *J Phys Chem C*, 2019, **123**, 26201–26210.
[57] Koch, C. Determination of core structure and point defect density along dislocations, PhD thesis (2002).